Biomembrane Adhesion to Substrates Topographically Patterned with Nanopits

Jaime Agudo-Canalejo, Dennis E. Discher

Biomembrane Adhesion to Substrates Topographically Patterned with Nanopits

Jaime Agudo-Canalejo[1,2,3,*] and Dennis E. Discher[4]

[1]Theory & Bio-Systems Department, Max Planck Institute of Colloids and Interfaces, 14476 Potsdam, Germany

[2]Rudolf Peierls Centre for Theoretical Physics, University of Oxford, Oxford OX1 3PU, UK

[3]Department of Chemistry, The Pennsylvania State University, University Park, PA 16802, USA

[4]Biophysical Engineering, University of Pennsylvania, Philadelphia, PA 19104, USA

[*]Correspondence: jaime.agudocanalejo@physics.ox.ac.uk

ABSTRACT We examine the adhesion of biomembranes to substrates topographically patterned with concave nanopits, and identify several universal features in the adhesion process. We find three distinct states, depending on whether the membrane remains flat above the nanopit, partially enters it, or completely adheres to it, and derive analytical conditions for the stability of these states valid for a very general class of nanopit shapes. Surprisingly, completely adhered states are always (meta)stable. We also show that the presence of many nanopits can increase or decrease the effective adhesiveness of a substrate, depending on the tension of the membrane and the strength of the membrane–substrate attraction. Our results have implications regarding several experimental methods which involve the formation of supported lipid bilayers on substrates patterned with nanopits, as well as observations of decreased spreading of cells and migration of cells towards regions of lower nanopit density on topographically patterned substrates. Furthermore, our predictions can also be directly tested in experiments exploring the adhesion of micropipette-aspirated giant vesicles to such substrates.

Introduction

Thanks to the advances of nanotechnology, it is now possible to fabricate solid substrates of very precise topography, with control over nanoscale features as small as 3 nm in the case of electron beam lithography. (1) These topographically patterned substrates are widely used in biophysical research as customizable, synthetic approximations to the nanoscale topography of the extracellular matrix that surrounds living cells. (2, 3) Topographies commonly investigated include spatial patterns of elongated nanogrooves, convex nanoposts, or concave nanopits on otherwise planar substrates. Variations in the shape and areal density of these features have been shown to strongly affect cell spreading, differentiation, migration, and proliferation. (3–11)

Although some theoretical effort has been dedicated to understanding the interaction of biomembranes with rough substrates (12, 13) as well as with undulated substrates patterned with nanogrooves (14), the interaction of biomembranes with substrates patterned with nanopits is still not understood. Cells in contact with nanopit-patterned substrates have been shown to display decreased adhesion and spreading in a number of experiments, see Ref. 3 for a review. Cells in such substrates have also been observed to migrate towards regions of lower nanopit density. 6 Moreover, substrates patterned with nanopits are useful not only in experiments with biological cells, but also in more basic biophysical research. In recent years, supported lipid bilayers grown on substrates patterned with concave nanopits (15, 16) have been used as platforms for single-molecule spectroscopy of membrane-embedded proteins, (17) as well as for the study of membrane curvature sensing by proteins. (18)

Given the wide relevance of nanopit-patterned substrates, it is surprising that a basic understanding of the underlying membrane–nanopit interaction is still lacking. Here, we intend to provide a comprehensive theory taking into account both the detailed interactions of the membrane with a single nanopit, as well as the collective effect of many nanopits on membrane adhesion, see Fig. 1. A membrane bound to such a patterned substrate, be it a cell, a giant vesicle, or a supported bilayer, will necessarily be bound to the planar surface of the substrate, see Fig. 1 (a), but it may or may not adhere to the surface of the nanopits, see Fig. 1(b). In fact, three qualitatively different states of the membrane can be distinguished, namely a non-adhered state (NA) if the membrane remains flat above

Figure 1: (a) A vesicle or cell (blue) and a supported bilayer (brown) adhere to a planar substrate topographically patterned with many concave nanopits, that may be distributed in any arbitrary manner. (b) Side-view displaying the geometry of a membrane adhering to a single smooth axisymmetric nanopit, with radius R and depth h. The membrane is said to be non-adhered (NA, red) if the position of the contact line between the bound and unbound membrane segments satisfies $r^*=R$, partially-adhered (PA, yellow) if $0 < r^* < R$, and completely adhered (CA, green) if $r^* \to 0$.
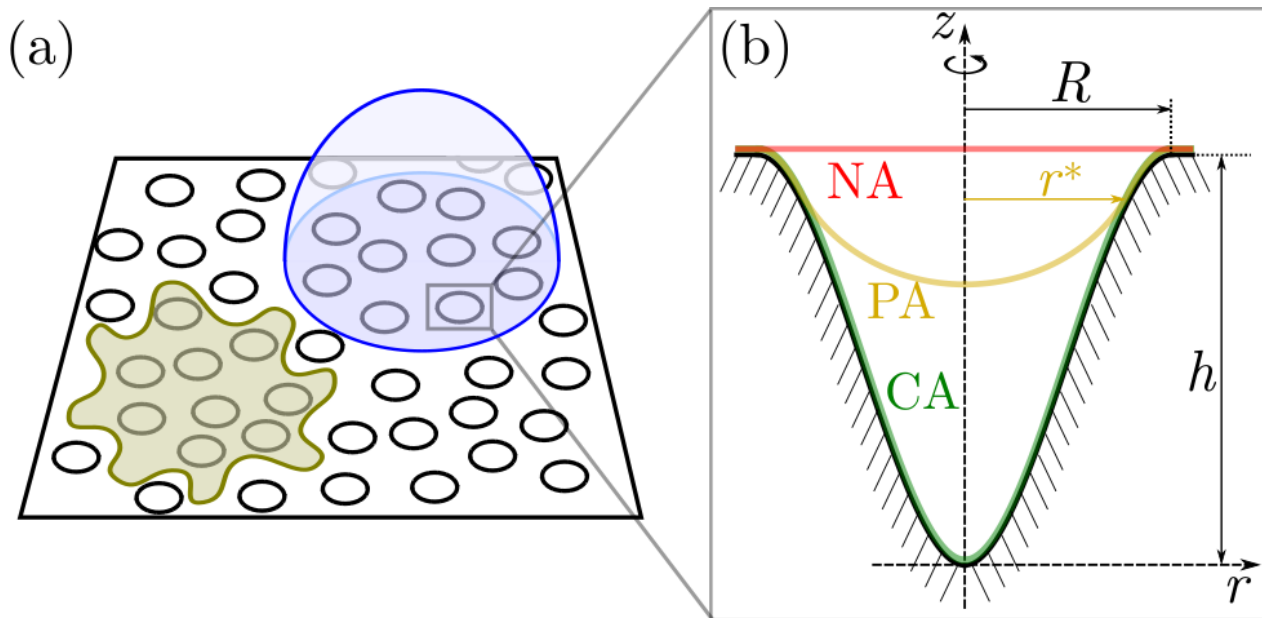
the nanopit, a partially-adhered state (PA) if the membrane only shallowly enters the nanopit, and a completely-adhered state (CA) if the membrane is fully bound to the nanopit and closely follows its shape.

We will first examine the stability of these three states for a single nanopit, using both numerical computations, as well as analytical calculations. The analytical calculations show that the general features of the adhesion process are universal, i.e. independent of the detailed shape of the nanopit, which may range from a shallow concavity to a deep cylindrical pit with vertical walls. Then, we will use these results to describe the coarse-grained effect of many nanopits on membrane–substrate adhesion. We will show that the presence of many nanopits endows the substrate with an 'effective adhesiveness', which depends on the tension of the membrane and on the actual adhesive strength of the membrane–substrate attraction. We will relate our results to experiments in the literature concerning cells and supported lipid bilayers in contact with substrates patterned with nanopits, describe how our predictions might be tested in future experiments using micropipette-aspirated giant vesicles, and discuss how the presence of the nanopits might affect the integrity of the membrane, as well as its lateral organization in the case of multicomponent membranes. We finish with a discussion of membrane adhesion to nanopits with more general, complex shapes.

Methods

Curvature elasticity model

Because the typical size of nanopits is several tens of nanometers or larger, (3, 18) many times larger than the membrane thickness, the membrane can be described within the theory of curvature elasticity. (19, 20) Its total energy is then given by

$$E = 2\kappa \int M^2 \mathrm{d}A - |W| A_{\mathrm{bo}} + \Sigma A. \qquad (1)$$

The first term in Eq. 1 corresponds to bending, where κ is the bending rigidity and M the mean curvature of the membrane at each point, with $M \equiv (C_1 + C_2)/2$, where C_1 and C_2 are the two principal curvatures. We will focus on symmetric bilayers without spontaneous curvature, and the contributions of Gaussian curvature to the energy can be ignored because we do not consider any changes of the topology of the membrane. (19) The second term represents the adhesion energy, which is included *via* a contact potential where $|W|$ is the adhesive strength of the membrane–substrate interactions and A_{bo} the area of membrane bound to the substrate. Finally, the third term represents the energetic cost of extracting an amount A of membrane area from a membrane reservoir at constant tension Σ. Such a reservoir is provided, for example, by the aspirated part of the membrane in the case of micropipette-held vesicles, or by the supported membrane itself in the case of supported lipid bilayers, in which case the tension is equal to the adhesive strength, $\Sigma = |W|$. Biological cells, on the other hand, have internal membrane reservoirs which are actively maintained at a constant tension. (21, 22)

Osmotic pressure contributions to the energy in Eq. 1 are negligible if the nanopits are much smaller than the cell or vesicle, and we further assume that there is enough space (a couple of nm) between membrane and substrate for the aqueous medium to freely flow in and out of nanopits. We also note that, in the case of cells, interactions with nanopits larger than a few hundred nanometers will necessary involve rearrangements of the cellular cortex underlying the lipid bilayer. The theoretical results described here are therefore expected to be valid only for nanopit sizes in the range of tens to a couple hundred nanometers in the case of biological cells and giant vesicles, but should remain valid for pits of any size in the case of supported bilayers.

Defining the shape of a nanopit

We rigorously define a smooth axisymmetric nanopit of radius R by a height function $z_{\mathrm{np}}(r)$, defined on the interval $0 \le r \le R$, that (i) is non-decreasing with only one inflection point in its

Figure 2: Geometry of a cylindrical nanopit, composed of a toroidal rim of radius R_{rim}, a vertical wall which corresponds to a cylindrical segment with radius R_{wall} and length L, and a hemispherical bottom segment with radius R_{wall}. In this particular example, the membrane (yellow) is in a partially adhered (PA) state, with the contact line located at the vertical wall.
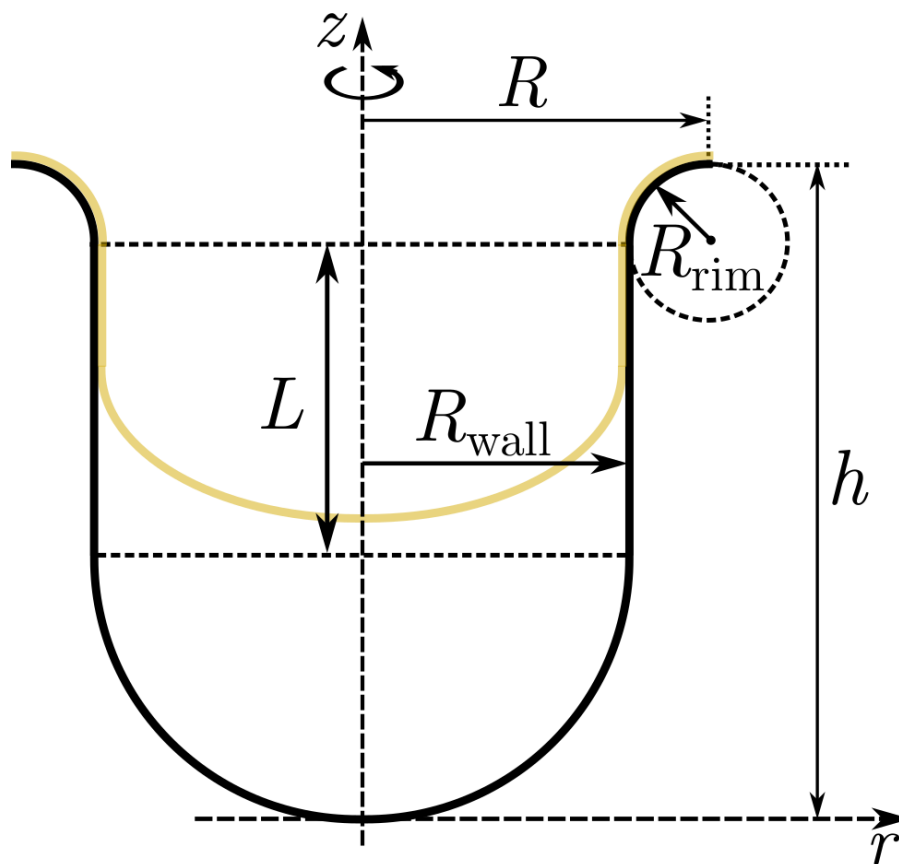
domain, (ii) is differentiable at least once, and satisfies (iii) $z'_{np}(0) = 0$ and (iv) $z'_{np}(R) = 0$. The first condition ensures that the nanopit has a simple shape with a single minimum at $r = 0$, while the latter three ensure that there aren't any 'kinks' along the nanopit contour, at its bottom, or at the matching line between the nanopit and the planar substrate, respectively. An example for such a height function, which we will use throughout this work, is the polynomial

$$z_{np}(r) = h\left[3(r/R)^2 - 2(r/R)^3\right] \qquad (2)$$

which is plotted in Fig. 1(b) for $h/R = 2$.

Besides the general class of nanopit shapes that can be fully described by a height function $z_{np}(r)$ satisfying the four conditions above, we will also consider the extreme case of *cylindrical* nanopits with vertical walls. These constitute a singular kind of nanopit, in that they cannot be completely described by a height function $z_{np}(r)$, because such a height function would be non-differentiable at the position of the wall $r = R_{wall}$, with $z'_{np}(r = R_{wall}) \to \infty$. As a typical example of such a cylindrical nanopit, we will consider piece-wise defined nanopits such as the one depicted in Fig. 2. Such a nanopit is composed of three distinct segments: a toroidal rim of radius R_{rim} that meets smoothly with the planar part of the substrate, a vertical wall corresponding to a cylindrical segment of radius R_{wall} and length L, and a bottom segment corresponding to a hemisphere of radius R_{wall}. In line with the notation above for general nanopits, the radius of the nanopit is then given by $R = R_{wall} + R_{rim}$, and its total height is $h = R_{wall} + L + R_{rim}$.

Throughout this work, we will focus on nanopits with shapes that satisfy the basic conditions of axisymmetry and smoothness just described. The relevance of these conditions will be highlighted in the last subsection of the *Discussion*, in which we will consider membrane adhesion to nanopits with more general shapes that do not satisfy some these conditions.

Energy landscapes and contact curvature condition

Using the standard shooting method for axisymmetric membranes, (19) we can numerically calculate the shapes of the unbound membrane segment that minimize the energy in Eq. 1 while smoothly matching the bound segment at any given contact radius $r = r^*$. In this way, we can obtain the energy landscapes $E(r^*)$ describing the adhesion of the membrane to the nanopit. We say that the NA state is (meta)stable if the energy $E(r^*)$ has a boundary minimum at $r^* = R$, the CA state is (meta)stable if $E(r^*)$ has a boundary minimum at $r^* = 0$, and a PA state is (meta)stable if $E(r^*)$ has a local minimum at some value $0 < r^* < R$. When the energy $E(r^*)$ has two minima, this corresponds to the coexistence of two (meta)stable states. In this case, the one with lowest energy of the two is said to be stable, while the other one is said to be metastable. When two (meta)stable states coexist, $E(r^*)$ will also have a maximum between these two minima, corresponding to the top of the barrier between the two (meta)stable states. We call this a transition state.

Alternatively, it is also possible to directly obtain the r^*-values of all the equilibria present in such an energy landscape, i.e. all the (meta)stable and transition states, without having to calculate the full energy landscape. Indeed, in equilibrium, a subtle balance between stresses and moments at the contact line (20, 23) relates the principal curvature of the unbound segment of the membrane perpendicular to the contact line, $C_\perp(r^*)$, to the curvature of the nanopit at the same line $C_{\perp,np}(r^*)$ via $C_\perp(r^*) = \sqrt{2|W|/\kappa} + C_{\perp,np}(r^*)$, or equivalently

$$|W| = \kappa \left[C_\perp \left(r^* \right) - C_{\perp, \mathrm{np}} \left(r^* \right) \right]^2 / 2. \qquad (3)$$

In this case, one can simply obtain $C_\perp \left(r^* \right)$ using the shooting method described above, and then introduce this value into Eq. 3 to obtain the equilibrium values of r^*, which include both (meta)stable as well as transition states, as a function of the adhesive strength $|W|$. By considering how the equilibrium r^*-values change with $|W|$ (and knowing that NA and CA states should be energetically preferred at low and high $|W|$, respectively) one can obtain the conditions under which NA, PA, or CA states are (meta)stable or become unstable, without the need to examine the energy landscapes explicitly.

Small gradient approximation

The shape of the unbound membrane $z(r)$ in contact with an axisymmetric nanopit described by a height function $z_{\mathrm{np}}(r)$ can be obtained analytically in the small gradient approximation $z'(r) \quad 1$. The general axisymmetric solution is (24)

$$z(r) \approx a_1 + a_2 \log \left(r / \lambda \right) + a_3 K_0 \left(r / \lambda \right) + a_4 I_0 \left(r / \lambda \right) \quad (4)$$

where $\lambda \equiv \sqrt{\kappa / \Sigma}$, and $I_\alpha (x)$ and $K_\alpha (x)$ are modified Bessel functions of the first and second kind, respectively. The constants a_i are defined by imposing membrane smoothness at $r = 0$ and $r = r^*$, leading to

$$z(r) - z(0) \approx \left[-1 + I_0 \left(r / \lambda \right) \right] \lambda z'_{\mathrm{np}} \left(r^* \right) / I_1 \left(r^* / \lambda \right) \quad (5)$$

with $0 \leq r \leq r^*$, and the small gradient approximation remaining valid whenever $z'_{\mathrm{np}} \left(r^* \right) \quad 1$.

Within this approximation, $C_\perp (r) \approx z''(r)$ and $C_{\perp, \mathrm{np}} (r) \approx z''_{\mathrm{np}} (r)$. The contact curvature condition in Eq. 3 can then be written explicitly as

$$|W| \approx \frac{\kappa}{2} \left(\frac{I_0 \left(r^* / \lambda \right) + I_2 \left(r^* / \lambda \right)}{2 \lambda I_1 \left(r^* / \lambda \right)} z'_{\mathrm{np}} \left(r^* \right) - z''_{\mathrm{np}} \left(r^* \right) \right)^2 . \quad (6)$$

Curvature of a membrane in contact with a vertical wall

In the particular case of cylindrical nanopits with a vertical wall, it is possible to calculate exactly the curvature $C_\perp (r^* = R_{\mathrm{wall}})$ of the membrane at the contact line where the membrane meets the wall. Indeed, suppose that the membrane is in an equilibrium state in which the contact line is located at the vertical wall, see Fig. 2. Because the shape of the unbound segment of the membrane does not depend on the height of the contact line along this wall (i.e., on how deep into the nanopit the membrane is), the energetic cost of moving this contact line up or down will be determined only by the energy of the bound segment. The energetic cost of moving the contact line downwards a distance δz is therefore

$$\delta E = \left(\frac{2\kappa}{\left(2 R_{\mathrm{wall}} \right)^2} - |W| + \Sigma \right) 2 \pi R_{\mathrm{wall}} \delta z . \qquad (7)$$

This energetic cost will be zero, and thus the membrane will be in equilibrium, if the adhesion contribution to the energy can compensate for both the bending and tension contributions, with

Figure 3: (a) Equilibrium radius of the contact line r^* as a function of adhesive strength $|W|$, for varying values of membrane tension Σ; and (b) Stability diagram displaying the coexistence of non-adhered (NA), partially-adhered (PA), and completely-adhered (CA) states as a function of $|W|$ and Σ. The nanopit shape is given by Eq. 2 with $h/R = 0.1$, which is plotted in the inset of (a). In (a), solid and dashed colored lines represent (meta)stable and transition PA states, respectively; the dashed black lines correspond to the small gradient approximation in Eq. 6; grey horizontal lines at $r^* = 1$ and $r^* = 0$ represent (meta)stable NA and CA states, respectively; and the vertical dotted lines mark the discontinuous transitions D at which NA states (red and blue) or PA states (green) switch metastability with CA states. In (b), the stability lines L_{na} and L_{pa} meet at a triple point indicated by the blue asterisk; the red dotted line is the large tension limit of L_{pa}; the eight green crosses correspond to the eight energy landscapes in Fig. 4; and the three colored arrows refer to the $|W|$-values in Fig. 6(a).
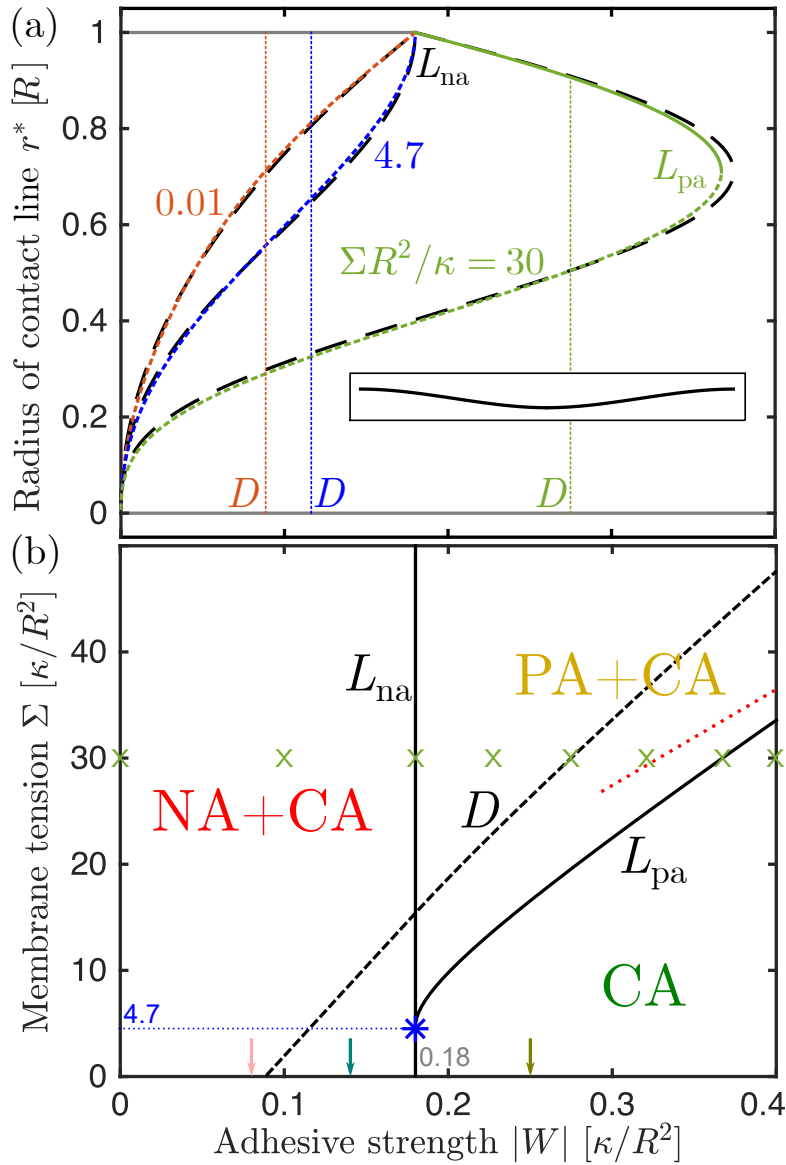
Figure 4: Energy landscapes of adhesion $\Delta E\left(r^{*}\right) \equiv E\left(r^{*}\right) - E(R)$, for the nanopit in Fig. 3, for membrane tension $\Sigma R^{2} / \kappa = 30$ and eight different values of the adhesive strength $|W|$, corresponding to the eight crosses in the stability diagram of Fig. 3(b). It can be directly seen that, for all values of $|W|$, the CA state at $r^{*} = 0$ is (meta)stable. With increasing $|W|$, the system crosses first the instability line L_{na} of the NA state (with $r^{*} = R$) towards a PA state (with $r^{*} \hat{\ } R$), then the discontinuous transition D where the PA and CA states switch metastability, and finally the instability line L_{pa} of the PA state towards the CA state.
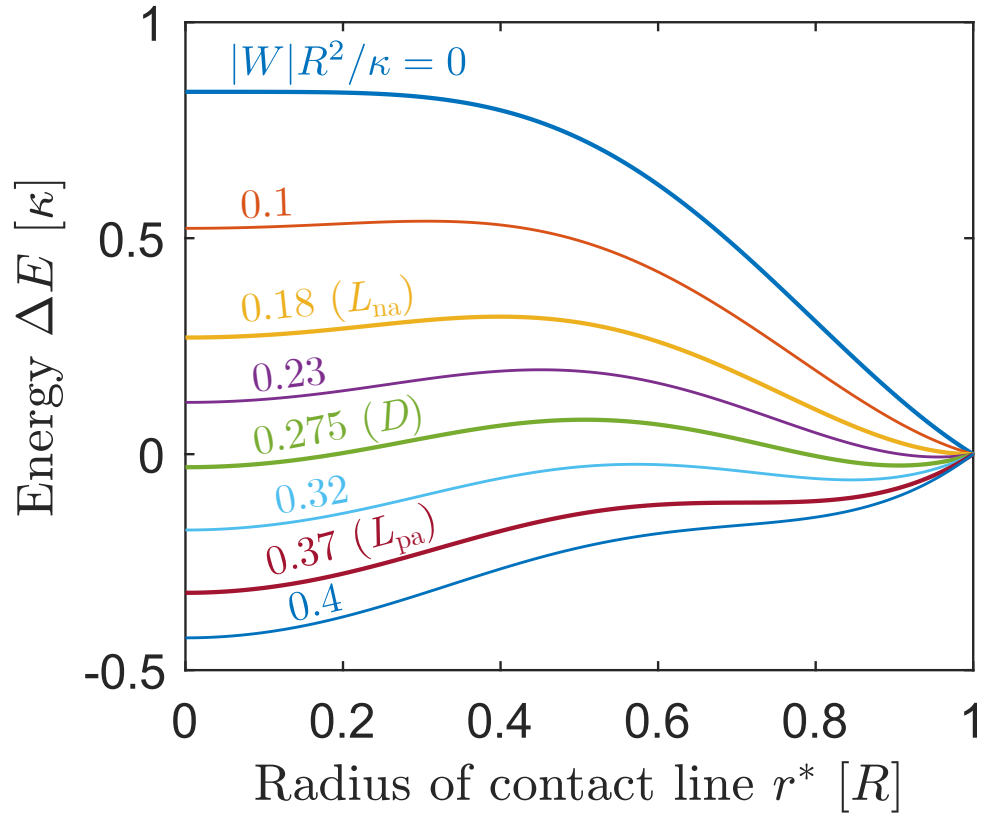
$$|W| = \Sigma + \frac{\kappa}{2R_{wall}^2}. \qquad (8)$$

Eq. 8 represents an equilibrium condition valid for the particular case in which the substrate–membrane contact line is at a vertical wall. However, in such a situation the membrane must also satisfy the general equilibrium condition in Eq. 3. Putting both equations together, and noting that at the vertical wall we have $C_{\perp,np}(r^* = R_{wall}) = 0$, we conclude that the curvature of the membrane at the contact line with the wall is

$$C_\perp(r^* = R_{wall}) = \sqrt{\frac{2\Sigma}{\kappa} + \frac{1}{R_{wall}^2}}. \qquad (9)$$

Results

Membrane interaction with a single nanopit

Let us first consider the interaction of the membrane with a single nanopit. In Fig. 3(a), we plot the numerically calculated equilibrium contact radius r^* of the membrane as a function of the adhesive strength $|W|$, for an example nanopit with shape given by Eq. 2 with $h/R = 0.1$, for three representative values of membrane tension Σ. The curves show that CA states are always (meta)stable, for all values of $|W|$ and Σ, and that the transition from NA or PA to CA states is always discontinuous. For low tension, we find that increasing $|W|$ leads to an instability L_{na} of NA states towards CA states, whereas for tensions above a critical value $\Sigma \approx 4.7\kappa/R^2$, NA states first transition continuously towards PA states, which then undergo an instability L_{pa} towards CA states for even higher values of $|W|$. The value of $|W|$ corresponding to the instability L_{na} is found to be independent of membrane tension, and is given by $|W| \approx 0.18\kappa/R^2$. At the discontinuous transitions D, marked by vertical lines, the NA or PA states have equal energy as the CA states. These results are summarized in the corresponding stability diagram in Fig. 3(b), describing the stability of NA, PA, and CA states as a function of $|W|$ and Σ. The features just described can also be seen in the energy landscapes that we display in Fig. 4, corresponding to the case of a membrane with tension $\Sigma = 30\kappa/R^2$ and eight different values of the adhesive strength $|W|$, which correspond to the eight crosses in Fig. 3(b). In particular, one can directly see in the energy landscapes that the CA state is (meta)stable for all values of $|W|$, as well as how the discontinuous transition D and the instability lines of the NA and the PA states are crossed with increasing adhesive strength.

The small gradient approximation in Eq. 6 is plotted as the black long-dashed lines in Fig. 3(a). This approximation works very well for shallow nanopits such as the one in Fig. 3(a), but becomes increasingly inaccurate for deeper nanopits with higher h/R and ultimately breaks down for nanopits with vertical walls (see next subsection). Importantly, however, the approximation in Eq. 6 can make *exact* predictions regarding the stability limits of the CA state ($r^* = 0$) and the NA state ($r^* = R$), because in these two limits the unbound membrane segment becomes exactly flat with $z'(r) \equiv 0$, independently of the nanopit depth.

In fact, we will now use Eq. 6 to show that the defining features of the membrane–nanopit interaction in Fig. 3 are universal, i.e. independent of the specific shape of the nanopit, as long as this shape satisfies the conditions described in the subsection *Defining the shape of a nanopit* of the *Methods*. First, let us evaluate Eq. 6 at $r^* = 0$. This requires some care, because $[I_0(x) + I_2(x)]/I_1(x)$ behaves as $2/x + O(x)$ around $x = 0$. The limit when $r^* \to 0$ of the first term inside the parenthesis can then be calculated as

$$\lim_{r^* \to 0} \frac{I_0\left(r^*/\lambda\right) + I_2\left(r^*/\lambda\right)}{2\lambda I_1\left(r^*/\lambda\right)} z'_{np}\left(r^*\right) = \lim_{r^* \to 0} \frac{1}{r^*} z'_{np}\left(r^*\right) = \lim_{r^* \to 0} \frac{1}{r^*}\left[z'_{np}\left(r^*\right) - z'_{np}\left(0\right)\right] = z''_{np}\left(0\right)$$

(10)

where we have used the condition that $z'_{np}\left(0\right) = 0$. Substituting this into Eq. 6, we finally find

$$|W| = 0 \qquad (11)$$

which implies that, for axisymmetric nanopits with a smooth bottom (no kink), the CA state is a solution for vanishing adhesion and is *always* (meta)stable, for any value of the adhesive strength, membrane tension, and independently of the detailed shape of the nanopit.

Second, for $r^* = R$ the first term inside the parenthesis in Eq. 6 vanishes and we find

$$|W| = \kappa z''_{np}(R)^2 / 2 = \kappa C_{rim}^2 / 2 \quad (12)$$

which defines the stability limit L_{na} of the NA state, and is indeed independent of membrane tension. This critical value of $|W|$ is however strongly dependent on the curvature of the nanopit rim $z''_{np}\left(R\right) = C_{\perp,np}\left(R\right) = C_{rim}$. If the nanopit meets the planar substrate with $C_{rim} = 0$, i.e. without a curvature discontinuity, the NA state is unstable even for vanishing adhesion. For the example in Fig. 3, Eq. 12 with $z''_{np}\left(R\right) = -6h/R^2$ predicts $|W| = 18\kappa h^2/R^4$, resulting in $|W|R^2/\kappa = 0.18$ for $h/R = 0.1$, which coincides with the numerical result in Fig. 3. We note that Eq. 12 could have been directly obtained from the contact curvature condition in Eq. 3, without recurring to the small gradient approximation, by noticing that in the NA state we have $C_\perp\left(R\right) = 0$ and $C_{\perp,np}\left(R\right) = C_{rim}$.

Third, using Eq. 6, we can find a condition for the existence of a (meta)stable PA state by imposing that $d|W|/dr^*\big|_{r^*=R} < 0$. The condition reads

$$\frac{1}{2}\frac{R}{\lambda}\frac{I_0\left(R/\lambda\right) + I_2\left(R/\lambda\right)}{I_1\left(R/\lambda\right)} z''_{np}\left(R\right) - Rz'''_{np}\left(R\right) < 0 \qquad (13)$$

and, taking into account that $z''_{np}\left(R\right)$ is always negative, and that $x[I_0\left(x\right) + I_2\left(x\right)]/I_1\left(x\right)$ is a monotonically increasing function for $x > 0$, defines a critical value of R/λ, and therefore of the membrane tension through $1/\lambda \equiv \sqrt{\Sigma/\kappa}$, above which (meta)stable PA states exist. For the example in Fig. 3(a-b), with $z'''_{np}\left(R\right) = -12h/R^3$, we find $R/\lambda \approx 2.17$, which means that the triple point at which the L_{na} and L_{pa} lines meet is located at $\Sigma R^2/\kappa \approx 2.17^2 \approx 4.7$, coinciding with the numerical result in Fig. 3. Remarkably, the condition in Eq. 13 is invariant under the vertical scaling transformation $z_{np}\left(r\right) \to \alpha z_{np}\left(r\right)$, which implies that the critical tension remains the same if the shape of a nanopit is vertically 'stretched' ($\alpha > 1$) or 'compressed' ($0 < \alpha < 1$). For example, both the deep nanopit in Fig. 1(b) and the shallow nanopit in the inset of Fig. 3(a) have the same critical tension given by $\Sigma R^2/\kappa \approx 4.7$. This is because both are described by the same height function in Eq. 2, the former with $h/R = 2$, the latter with $h/R = 0.1$, and therefore both are related by a vertical scaling transformation. Furthermore, by evaluating Eq. 13 at $R/\lambda = 0$, we find the condition

$$z''_{np}\left(R\right) - Rz'''_{np}\left(R\right) < 0 \quad (14)$$

for PA states to exist for all values of $\Sigma \geq 0$, that is, nanopits that satisfy Eq. 14 will not display a triple point in their stability diagram.

Finally, let us examine the limit of large membrane tension, with $\Sigma R^2 / \kappa \gg 1$. In this limit, bending is negligible and the membrane will behave as a flat liquid interface satisfying the Young-like equation $|W| \approx \Sigma (1 - \cos \theta)$, where $\theta = \arctan z'_{\text{np}} (r^*)$ is the angle between the substrate and the horizontal plane at the contact line r^*. First, notice that the function $1 - \cos(\arctan x)$ is monotonically increasing for $x > 0$. Second, the function $z'_{\text{np}} (r^*)$ will have a maximum at the value $r^* = r_{\text{in}}$ at which the height function $z_{\text{np}} (r^*)$ has an inflection point, i.e. when $z''_{\text{np}} (r^* = r_{\text{in}}) = 0$. The PA state will become unstable towards the CA state for adhesive strengths larger than the maximum of $|W|$ as a function of r^*, which is given by

$$|W| \approx \Sigma \{1 - \cos[\arctan z'_{\text{np}} (r_{\text{in}})]\} \qquad (15)$$

and represents the large tension behavior of the stability limit L_{pa}. For the nanopit in Fig. 3, we find $r_{\text{in}} = R / 2$ and $z'_{\text{np}} (r_{\text{in}}) = (3/2)(h/R)$, leading to $|W| \approx 0.011\Sigma$ which is plotted as the red dotted line in Fig. 3(b).

The interaction of a membrane with a nanopit of arbitrary shape (as long as this shape is axisymmetric and smooth, satisfying the conditions introduced in subsection *Defining the shape of the nanopit*) can therefore be universally described in the following way. The completely adhered (CA) state will be always at least metastable for all values of the adhesive strength $|W|$ or the membrane tension Σ. For low values of the adhesive strength $|W|$, lower than the tension-independent threshold given by Eq. 12, this CA state will coexist with the non-adhered (NA) state. For values of $|W|$ larger than this threshold, the NA state will typically become unstable towards a partially-adhered (PA) state, but it may also become unstable directly towards the CA state for certain nanopits if the membrane tension is low enough, see Eqs. 13–14. Even for large tensions, however, the PA state ultimately becomes unstable towards the CA state for large enough adhesive strengths, as approximated by Eq. 15 in the limit of large membrane tension.

Membrane interaction with a single cylindrical nanopit

An important class of nanopits corresponds to cylindrical nanopits with vertical walls, see Fig. 2. Cylindrical nanopits covered by a supported lipid bilayer have been used, for example, as waveguides for single-molecule spectroscopy of membrane-embedded proteins. (17) Such nanopits are particularly easy to produce and simple to describe, because their geometry is fully determined by their radius, their depth, and the curvature of their rim. Cylindrical nanopits with vertical walls represent an extreme, singular example of the general smooth axisymmetric nanopits that we have described above. One may thus wonder how the general results described above apply to cylindrical nanopits. In Fig. 5(a), we plot the numerically calculated equilibrium contact radius r^* of the membrane as a function of the adhesive strength $|W|$, for a cylindrical nanopit with cylinder radius $R_{\text{wall}} = 0.8R$, rim radius $R_{\text{rim}} = 0.2R$, and arbitrary wall length L, for a representative value of the membrane tension Σ. The corresponding stability diagram representing the stability of NA, PA, and CA states as a function of $|W|$ and Σ is depicted in Fig. 5(b). The discontinuous transition D at which NA or PA states switch metastability with CA states is not displayed in this case, because it does depend on the specific choice of wall length L.

As expected, the small gradient approximation in Eq. 6, which corresponds to the black long-dashed line in Fig. 5(a), completely breaks down in the proximity of the vertical wall when $r^* \approx R_{\text{wall}}$.

Nevertheless, it is still accurate in describing the stability of the CA and NA state, at $r^* = 0$ and $r^* = R$, respectively. Indeed, we first notice that the CA state is again (meta)stable for all values of the adhesive strength $|W|$ or the membrane tension Σ, as predicted by Eq. 11 above. Secondly, the

Figure 5: Interaction with a single cylindrical nanopit: (a) Equilibrium radius of the contact line r^* as a function of adhesive strength $|W|$, for tension $\Sigma R^2/\kappa = 10$ which is representative of all other values of the tension Σ; and (b) Stability diagram displaying the coexistence of non-adhered (NA), partially-adhered (PA), and completely-adhered (CA) states as a function of $|W|$ and Σ. The shape of the nanopit is determined by $R_{\text{wall}} = 0.8R$, $R_{\text{rim}} = 0.2R$, and arbitrary L, see Fig. 2. The meaning of all lines and symbols is the same as in Fig. 3. In contrast to the latter figure, we do not indicate the location of the discontinuous transition D, which would depend on the specific value of the wall height L. The meaning of the labels (i–iii), 'hs-wall', and 'wall-rim' in (a) is explained in the text.
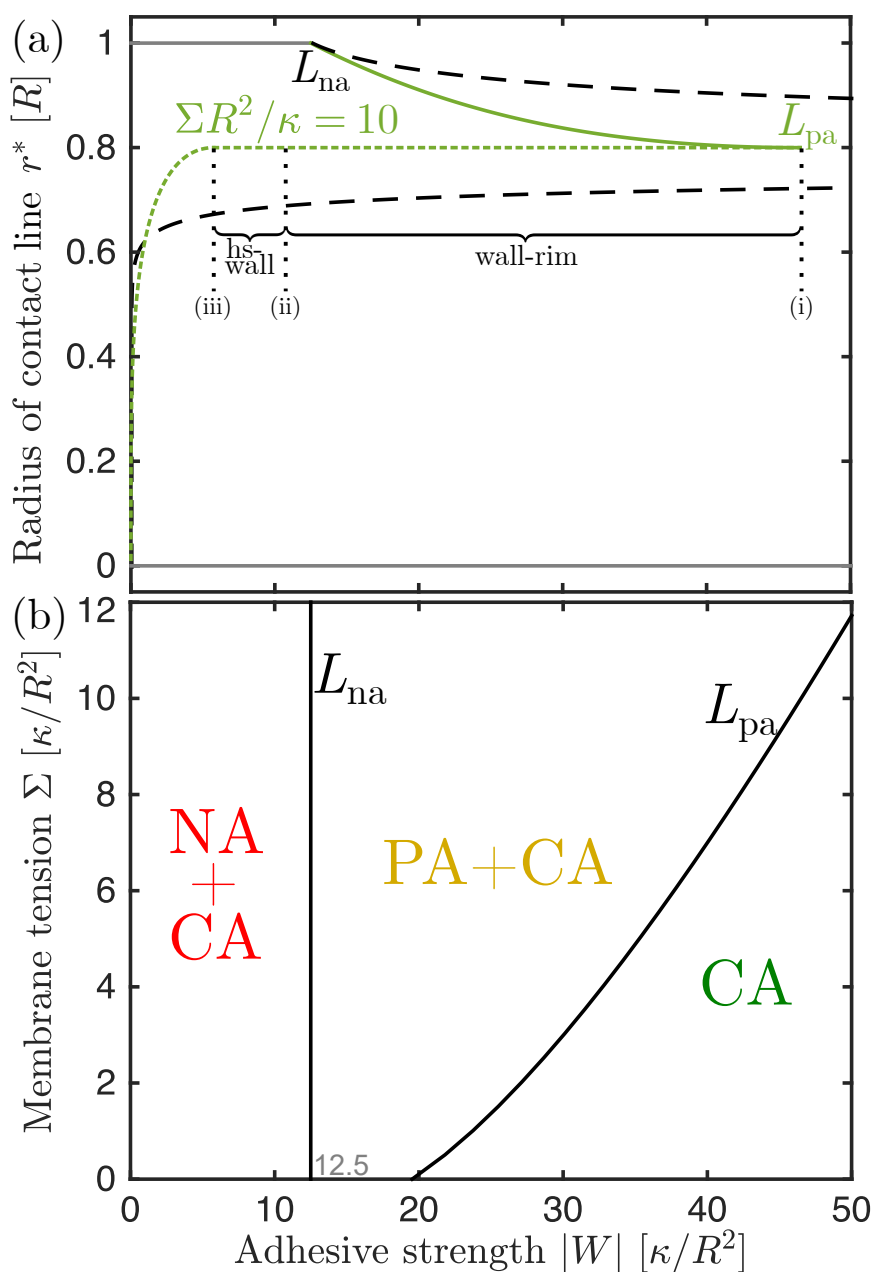
NA state again becomes unstable for sufficiently large values of the adhesive strength $|W|$, beyond the tension-independent stability line L_{na}. As predicted by Eq. 12 with $z_{\mathrm{np}}''(R) = C_{\mathrm{rim}} = -1/R_{\mathrm{rim}}$, the stability line L_{na} is in this case given by

$$|W| = \frac{\kappa}{2R_{\mathrm{rim}}^2} \qquad (16)$$

which leads to $|W|R^2/\kappa = 12.5$ for $R_{\mathrm{rim}} = 0.2R$, coinciding with the numerical result in Fig. 5. The minimal adhesive strength required for the NA state to become unstable is therefore strongly dependent on the curvature of the rim, and becomes larger as the rim becomes more strongly curved, i.e. sharper.

Inspection of the stability diagram in Fig. 5(b) shows that, for cylindrical nanopits, there is no triple point such as the one in Fig. 3(b). That is, in the case of cylindrical nanopits, the NA state will always become unstable towards a PA state, even for vanishing membrane tension. This may have been predicted using the condition for the absence of a triple point derived above, see Eq. 14. For cylindrical nanopits as discussed here we have $z_{\mathrm{np}}''(R) = C_{\mathrm{rim}} = -1/R_{\mathrm{rim}}$ and $z_{\mathrm{np}}'''(R) = 0$, and the condition in Eq. 14 reads $-1/R_{\mathrm{rim}} < 0$, which is always satisfied.

One may have thought that nanopits with vertical walls would be less analytically tractable than those without them, given that the small gradient approximation in Eq. 6 completely breaks down at the wall. This is however not the case, and in fact an exact expression for the stability limit of PA states L_{pa} can be derived for cylindrical nanopits. As described in *Methods*, one can derive an exact expression for the curvature of the membrane at the position of the contact line $C_{\perp}(r^* = R_{\mathrm{wall}})$ if this contact line is located at a vertical wall, see Eq. 9. Moreover, we note that a cylindrical nanopit such as the one in Fig. 2 displays three distinct curvatures along the vertical wall: (i) at the highest point where the rim meets the cylindrical segment the curvature is that of the rim, with $C_{\perp,\mathrm{np}}(r^* = R_{\mathrm{wall}}) = -1/R_{\mathrm{rim}}$; (ii) along the cylindrical segment, the curvature is $C_{\perp,\mathrm{np}}(r^* = R_{\mathrm{wall}}) = 0$; and (iii) at the lowest point where the hemispherical bottom segment meets the cylindrical segment the curvature is that of the hemisphere, with $C_{\perp,\mathrm{np}}(r^* = R_{\mathrm{wall}}) = 1/R_{\mathrm{wall}}$.

Now, combining Eq. 9 with Eq. 3, and introducing the three values (i–iii) for $C_{\perp,\mathrm{np}}(r^* = R_{\mathrm{wall}})$, we obtain three different values of the adhesive strength $|W|$, which correspond to the three dotted vertical segments in the example of Fig. 5(a). The largest of these three values, obtained from curvature (i), is given by

$$|W| = \frac{\kappa}{2}\left[\sqrt{\frac{2\Sigma}{\kappa} + \frac{1}{R_{\mathrm{wall}}^2}} + \frac{1}{R_{\mathrm{rim}}}\right]^2 \qquad (17)$$

and coincides exactly with the numerically-obtained instability line L_{pa} in Fig. 5. Remarkably, the instability of PA states towards CA states described by Eq. 17 is independent of the depth of the nanopit as defined by the wall length L, as well as of the specific shape of the nanopit bottom.

The values of $|W|$ obtained from curvatures (ii) and (iii) also have a physical meaning. For adhesive strengths in the interval obtained from (i) and (ii)

$$\frac{\kappa}{2}\left[\sqrt{\frac{2\Sigma}{\kappa} + \frac{1}{R_{\mathrm{wall}}^2}} + \frac{1}{R_{\mathrm{rim}}}\right]^2 > |W| > \Sigma + \frac{\kappa}{2R_{\mathrm{wall}}^2}, \qquad (18)$$

the transition state corresponding to the top of the energy barrier separating the NA or PA state from the CA state is represented by the state in which the contact line is located at the line where the rim and the vertical wall meet. This $|W|$-range is indicated by the label 'wall-rim' in Fig. 5(a). For adhesive strengths with $|W| = \Sigma + \kappa / 2R_{\text{wall}}^2$, corresponding to point (ii), the transition state is degenerate and the top of the energy barrier is a 'plateau' corresponding to the contact line being located anywhere along the wall of the nanopit. For adhesive strengths in the interval obtained from (ii) and (iii)

$$\Sigma + \frac{\kappa}{2R_{\text{wall}}^2} > |W| > \frac{\kappa}{2}\left[\sqrt{\frac{2\Sigma}{\kappa} + \frac{1}{R_{\text{wall}}^2}} - \frac{1}{R_{\text{wall}}}\right]^2 , \quad (19)$$

the transition state is represented by the state in which the contact line is located at the line where the hemispherical bottom segment and the vertical wall meet. This $|W|$-range is indicated by the label 'hs-wall' in Fig. 5(a). Finally, for even lower adhesive strengths the transition state will be represented by states where the contact line is somewhere along the hemispherical bottom segment.

In summary, the interaction of membranes with cylindrical nanopits of arbitrary radius, rim curvature, or depth can be described in the following way. As in the case of non-cylindrical nanopits, the completely adhered (CA) state will be always at least metastable for all values of the adhesive strength $|W|$ or the membrane tension Σ. For low values of the adhesive strength $|W|$, below the tension-independent threshold given by Eq. 16, this CA state will coexist with the non-adhered (NA) state. Surprisingly, this threshold value is independent of the nanopit radius or depth, and only depends on the radius of curvature of the rim. For values of $|W|$ larger than this threshold, the NA state becomes unstable towards a partially-adhered (PA) state, independently of the membrane tension. Finally, for adhesive strengths larger than the threshold given by Eq. 17, the PA state becomes unstable towards the completely-adhered (CA) state. This latter threshold is dependent on the tension of the membrane, but again does not depend on the depth of the nanopit. Moreover, these two important thresholds are independent of the shape of the bottom of the nanopit. The main results described here are therefore valid even if the bottom of the cylindrical nanopit has a shape other than hemispherical.

Effective adhesiveness of substrates patterned with many nanopits

Now that we understand the interaction of the membrane with single nanopits, we turn to the collective effect of many nanopits on membrane–substrate adhesion, see Fig. 1(a). Suppose that a membrane is in contact with the substrate over a 'projected' area A_{xy} on the horizontal plane, and that this projected area spans N nanopits. The total energy of the system is given by $E = (\Sigma - |W|)(A_{xy} - N\pi R^2) + NE_{\text{np},i}$, where $E_{\text{np},i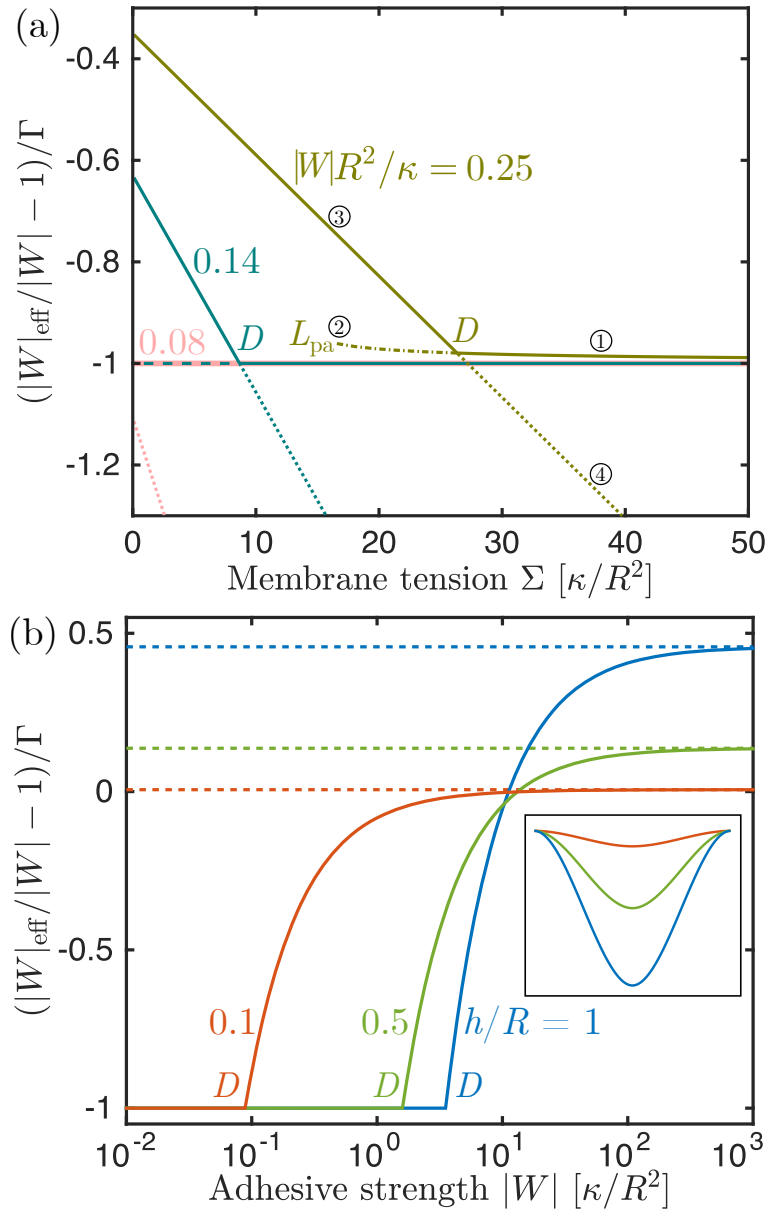}$ is the interaction energy with a single nanopit. The subindex i can take the values $i = \text{NA, PA, CA}$ corresponding to the three possible states of the membrane–nanopit complex, depending on which of these states are (meta)stable. We can now define the effective adhesiveness $|W|_{\text{eff}}$ of an equivalent, coarse-grained planar substrate without nanopits by rewriting the energy of the system as $E = (\Sigma - |W|_{\text{eff}})A_{xy}$. Equating both expressions, we obtain

$$|W|_{\text{eff}} = |W| + \Gamma\left(\Sigma - |W| - E_{\text{np},i} / \pi R^2\right) \qquad (20)$$

where $\Gamma \equiv N\pi R^2 / A_{xy}$ is the fraction of the projected area of the substrate that is covered in nanopits, which can range from $\Gamma = 0$ in the absence of nanopits to a maximum of $\Gamma = \pi / 2\sqrt{3} \approx 0.9$ for an optimal hexagonal packing of nanopits.

This effective adhesiveness, rescaled as $\left(|W|_{\text{eff}} / |W| - 1\right) / \Gamma$, is plotted in Fig. 6(a) for a substrate patterned with nanopits such as the one in Fig. 3, as a function of membrane tension, for the three

14

Figure 6: (a) Rescaled effective adhesiveness $|W|_{\text{eff}}$ for a substrate patterned with nanopits such as the one in Fig. 3(a), with $h/R = 0.1$, as a function of tension Σ, for three different values of the real adhesive strength $|W|$, corresponding to the three arrows in Fig. 3(b). Solid lines correspond to all nanopits being in the lowest energy state, which might be NA, PA, or CA; whereas dashed, dashed-dotted, and dotted lines correspond to metastable NA, PA, and CA states, respectively. The points 1–4 represent a hysteresis cycle of decreasing-increasing tension, as described in the text. (b) Rescaled $|W|_{\text{eff}}$ at $\Sigma = 0$ as a function of $|W|$, for the same type of nanopits as in (a) but for three different values of h/R. The corresponding nanopit shapes are depicted in the inset. Horizontal dashed lines indicate the asymptotes for large $|W|$ given by Eq. 23.

values of real adhesive strength $|W|$ indicated by the arrows in Fig. 3(b). In general, $|W|_{\text{eff}}$ decreases with increasing membrane tension. Because the membrane interactions with a single nanopit showed bistable behavior, with NA and CA, or PA and CA states sometimes coexisting, $|W|_{\text{eff}}$ can also show two coexisting branches. Solid lines correspond to every nanopit being in its lowest energy stable state, which in turn translates into higher values of $|W|_{\text{eff}}$. The lower values of $|W|_{\text{eff}}$, corresponding to all nanopits staying in metastable NA, PA or CA states, are plotted as dashed, dashed-dotted, and dotted lines, respectively.

The existence of bistable behavior should manifest itself as hysteresis in the observed adhesiveness when the membrane tension is increased or decreased. As an example, consider the case with $|W|R^2/\kappa = 0.25$ depicted in Fig. 6(a). Adhesion measurements at high tension, to the right of L_{pa}, are expected to explore the PA branch. If, however, once in contact with the substrate the tension of the membrane is sufficiently decreased (to the left of L_{pa}), the PA branch will become unstable and the system will fall into the CA branch with higher effective adhesiveness. Even if the tension is now increased back to its original value, the system will typically remain in the metastable CA branch, with effective adhesiveness lower than at the beginning of the cycle. The hysteretic cycle just described corresponds to the points 1–4 indicated in Fig. 6(a).

For NA states, the interaction energy with a single nanopit is simply $E_{\text{np,NA}} = \Sigma\pi R^2$, and Eq. 20 naturally predicts a *decreased* adhesiveness in the presence of nanopits, with $|W|_{\text{eff}} = |W|(1-\Gamma) < |W|$, or equivalently $(|W|_{\text{eff}}/|W|-1)/\Gamma = -1$. For PA states, we also find decreased adhesiveness, slightly larger but close to that of NA states, so that $(|W|_{\text{eff}}/|W|-1)/\Gamma \approx -1$. For CA states, on the other hand, the rescaled $|W|_{\text{eff}}$ depends strongly on both $|W|$ and Σ. Indeed, the interaction energy for a CA state can be written as $E_{\text{np,CA}} = (\Sigma - |W|)A_{\text{np}} + E_{\text{be,np}}$, where $A_{\text{np}} > \pi R^2$ is the surface area of the nanopit, and $E_{\text{be,np}} = 2\kappa\int_{A_{\text{np}}} M^2 dA > 0$ is the bending energy of the membrane adhering to it. Introducing $E_{\text{np,CA}}$ into Eq. 20, we find

$$\left(\frac{|W|_{\text{eff}}}{|W|}-1\right)\frac{1}{\Gamma} = \frac{(|W|-\Sigma)(A_{\text{np}}-\pi R^2)-E_{\text{be,np}}}{|W|\pi R^2} \qquad (21)$$

which increases both with increasing $|W|$ and with decreasing Σ. In fact, Eq. 21 predicts an *increased* adhesiveness in the presence of nanopits, with $|W|_{\text{eff}} > |W|$, whenever the numerator is positive, i.e. when

$$|W|-\Sigma > \frac{E_{\text{be,np}}}{A_{\text{np}}-\pi R^2} \qquad (22)$$

and a decreased adhesiveness otherwise. Furthermore, in the limit of very adhesive substrates with $|W|$ much larger than both Σ and κ/R^2, Eq. 21 predicts that the nanopit-induced increase in substrate adhesiveness saturates to

$$\left(\frac{|W|_{\text{eff}}}{|W|}-1\right)\frac{1}{\Gamma} \approx \frac{A_{\text{np}}}{\pi R^2}-1, \qquad (23)$$

which becomes larger with increasing nanopit depth.

To illustrate this behavior, we have plotted in Fig. 6(b) the rescaled $|W|_{\text{eff}}$ as a function of $|W|$, for $\Sigma = 0$ and three different values of h/R, i.e. of nanopit depth. We focus only on the stable branches, which are the NA branch for low adhesion and the CA branch for higher adhesion, beyond the discontinuous transition D. The asymptotes for large $|W|$ given by Eq. 23 are represented by the horizontal dashed lines. As predicted, for low $|W|$ the presence of nanopits acts to decrease the effective adhesiveness of the substrate, with $|W|_{\text{eff}} < |W|$, whereas for sufficiently high $|W|$ the nanopits increase surface adhesiveness, with $|W|_{\text{eff}} > |W|$. Furthermore, for low values of $|W|$, the effective adhesiveness decreases both with increasing nanopit depth as well as with increasing nanopit coverage Γ; the opposite is true for high values of $|W|$.

Discussion

Supported lipid bilayers

Supported lipid bilayers grown on substrates topographically patterned with nanopits have recently been proposed as platforms for single-molecule spectroscopy of membrane-embedded proteins, (17) as well as for the study of membrane curvature sensing by proteins. (18) In these experimental methods, it is essential that the supported bilayer closely follow the shape of the nanopits, i.e. be found in the CA state. It is therefore important to understand under which conditions we can expect to find CA states over NA or PA states.

The tension of a supported membrane is fixed by the adhesiveness of the substrate itself, with $\Sigma = |W|$. (25) This can be intuitively understood by realizing that, because the total membrane area of the supported bilayer is fixed, any new area δA brought into the nanopit was previously adhering to the flat part of the substrate, which implies an energetic cost $\delta E = +|W|\delta A$. In the case of supported bilayers, therefore, the adhesive strength and the membrane tension are not independent variables, and we can only explore one-dimensional cuts $\Sigma = |W|$ through the two-dimensional $(|W|, \Sigma)$ stability diagrams such as those in Figs. 3(b) and 5(b).

Supported lipid bilayers are typically grown by the adhesion and rupture of vesicles onto the substrate. (15, 16) Our results imply that how a supported bilayer in a CA state can be successfully generated will depend on the size of these vesicles, in particular, on whether the vesicles are smaller or larger than the size of the nanopit. First, let us consider the case of vesicles that are smaller than the nanopit. Rupture of the vesicles onto the surface of the nanopit will generate a CA state from the beginning, and the important question is then whether this initial CA state will remain stable. Luckily, our results above show that CA states are (meta)stable for *all* values of the adhesive strength $|W|$, and independently of the nanopit shape. It is therefore expected that supported bilayers in a CA state, i.e. closely following the shape of the nanopits, can be easily generated from the adhesion and rupture of sufficiently small vesicles onto the substrate, in the sense that the vesicles are small enough to enter the nanopit. Theoretical studies show that small vesicles can adhere to concave surfaces more easily than to flat surfaces. (26, 27)

Now, let us consider the case of supported membranes generated by the adhesion and rupture of vesicles that are larger than the nanopits, in the sense that they are too large to enter the nanopit. Rupture of such vesicles onto the substrate will lead to the initial formation of NA or PA states, and the important question is then whether or not these states will be unstable towards a CA state. Here, we find an interesting behavior. Inspection of Fig. 3(b), corresponding to a rather shallow and flat nanopit, shows that the line $\Sigma = |W|$ will cross the instability line L_{na} at $|W| = 0.18\kappa/R^2$ and remain below the instability line L_{pa} for all larger $|W|$-values. Therefore, any sufficiently large adhesive strength will spontaneously lead to a CA state for a supported membrane in contact with such nanopits. On the other hand, inspection of Fig. 5(b), corresponding to a cylindrical nanopit with vertical walls, shows that the line $\Sigma = |W|$ will cross the instability line L_{na} but not the instability

line L_{pa}, at least within the area of the figure. This implies that supported membranes in contact with such nanopits will remain in (meta)stable PA states even for very adhesive substrates with large $|W|$.

The transition between these two regimes can be understood from the limiting behavior of the instability line L_{pa} at large membrane tension, given by Eq. 15. Indeed, this equation can be rewritten as $\Sigma \approx \left\{1 - \cos[\arctan z'_{np}(r_{in})]\right\}^{-1} |W| \equiv \alpha |W|$. As long as the nanopit does *not* have vertical walls, we find $\alpha > 1$, and the line $\Sigma = |W|$ will eventually cross the instability line L_{pa}. As the walls of the nanopit are made more vertical, the value of α becomes closer to one, and the two lines become more parallel to each other, leading to an increase in the value of $|W|$ at which the two lines cross and the PA state becomes unstable for a supported membrane. Ultimately, for a nanopit with vertical walls, we find $\alpha = 1$, implying that the two lines become exactly parallel and do not cross for any $|W|$-value. Therefore, in the extreme case of nanopits with vertical walls (and only in this case), PA states will remain metastable for all values of the adhesive strength $|W|$. This can be seen explicitly by comparing $\Sigma = |W|$ with the exact expression of L_{pa} for cylindrical nanopits, see Eq. 17. For all other nanopits with non-vertical walls, there will be a value of $|W|$ above which both NA and PA states are unstable towards CA states.

After the vesicles (large or small) adhere and rupture onto the substrate, the different patches of membrane arising from this rupture process will spread and creep across the surface and stitch together into a uniform and continuous supported bilayer. (28) In the presence of nanopits, the energetics and dynamics of this 'coarsening' process will be rather subtle, and should depend on the relative size of the membrane patches (i) with respect to the size of the nanopits, as well as (ii) with respect to the typical distance between nanopits. As an example of (i), note that whereas a small membrane patch may 'sense' the local curvature of a nanopit larger than itself (small displacements of the patch will affect both its bending energy as well as the length of its edge, and therefore its edge energy (29)), a large membrane patch that covers a whole nanopit will be trapped in a degenerate metastable state. Small displacements of the patch will not affect its energy, as long as the nanopit is fully contained within the boundaries of the patch. As an example of (ii), note that a membrane patch that is smaller than the typical distance between nanopits may simply 'avoid' entering a nanopit if this is energetically unfavorable (we note, however, that entering a nanopit may also be energetically favorable: whereas the bending energy of the patch will necessarily increase, its edge energy may decrease if the length of the patch boundary is reduced in the process). A membrane patch that is larger than the typical distance between nanopits, however, may only 'avoid' a nanopit by deforming the shape of its boundary. If the energetic cost of this process is too large, it will be favorable for the membrane patch to instead spread over the nanopit, leading either to a NA, PA or CA state, depending on the adhesive strength of the substrate. All in all, we expect the coarsening process of supported lipid bilayers on substrates with complex topography to show a rich spectrum of behaviors.

Giant Unilamellar Vesicles

A different model system that can be used to experimentally test the theoretical results described here is provided by Giant Unilamellar Vesicles (GUVs). In the context of testing our experimental predictions, it is important to note that an isolated GUV has a fixed number of lipids on its membrane, and therefore a certain optimal area. The mechanical tension of its membrane is coupled to the lateral stretching or compression of the membrane above or below this optimal area. Therefore, for an isolated GUV, tension is not a fixed parameter, and instead depends in a complex manner on the shape and geometric constraints of the vesicle, as well as on the adhesiveness of the substrate. (30)

Alternatively, one may perform experiments using micropipette-held vesicles. In a micropipette setup, part of the GUV is aspirated (the 'tongue'), whereas the majority of the GUV remains outside the micropipette. By controlling the aspiration pressure, and therefore the length of the tongue, the tension of the membrane becomes an externally tunable control parameter. With respect to small

perturbations of the part of the GUV outside the micropipette, the membrane area stored in the tongue then behaves as a membrane reservoir at fixed tension Σ. (31)

Such a micropipette setup is ideal to explore the stability of NA, PA, and CA states as described here, see Figs. 3(b) and 5(b), because $|W|$ and Σ can be varied independently from each other. However, directly determining the specific state of a membrane in contact with a single nanopit may prove experimentally challenging. In this case, one could directly explore the effective adhesiveness $|W|_{\rm eff}$ of a substrate patterned with many such nanopits. Indeed, suppose that a micropipette-held GUV is pressed against a topographically patterned substrate in such a way that the vesicle–substrate contact area extends over a large number of nanopits. Measurements of the force required to detach the GUV from the substrate can then be used to gauge the effective adhesiveness $|W|_{\rm eff}$ of the substrate. (31–34)

Of particular interest will be to explore the effective adhesiveness of the substrate as a function of the tension of the membrane. As shown in Fig. 6(a), the effective adhesiveness is generally expected to decrease with increasing membrane tension. But not only that: due to the existence of bistable behavior with coexistence of NA and CA, or PA and CA branches, the system should exhibit hysteretic behaviour when subject to cycles of increasing and decreasing tension, as described above. One example of a hysteresis cycle of decreasing and increasing tension is depicted by the points 1–4 in Fig. 6(a). In the case of a micropipette-held GUV, this would correspond to decreasing and increasing the aspiration pressure.

We note that, in the present work, we have focused on the adhesion of vesicles to nanopits, i.e. pits that are much smaller than the vesicle, so that the vesicle-substrate contact region is expected to cover many such pits. The opposite situation, corresponding to a vesicle adhering to a concave pit of size comparable to or larger than the size of the vesicle, has also been studied theoretically. (26, 27) In the latter works, it was shown that the critical adhesive strength necessary for binding of the vesicle to the substrate is lower in concave pits than in flat substrates.

Biological cells

The adhesion of biological cells to substrates topographically patterned with nanopits has been explored in a number of experiments. (3–10, 15–18) A common observation in the majority of these experiments has been a decrease in cell spreading in the presence of nanopits with respect to the same substrate in the absence of nanopits, see Ref. 3 for a review. Another particularly interesting observation, in Ref. 6, is that cells tend to migrate towards regions of lower nanopit density.

Both types of observations seem to suggest that in these experiments the presence of nanopits caused a reduction of the effective adhesiveness of the substrate, with $|W|_{\rm eff} < |W|$. Our findings imply, see Eq. 22 and Fig. 6(b), that these trends may be reversed in more sticky substrates with larger adhesive strength $|W|$, as well as for cells with lower membrane tension Σ. Alternatively, it may be possible to engineer the shape of the nanopits in order to make the right hand side of Eq. 22 as small as possible, so as to minimize the critical value of the adhesive strength above which nanopits begin to enhance the effective adhesiveness of the substrate. In regard to this we note that, as can be inferred from Fig. 6(b), this critical value of $|W|$ is only very weakly dependent on the depth of the nanopit (i.e. on the value of h/R), and instead depends more strongly on the finer details of the nanopit shape.

Membrane rupture and defect formation

Troughout the paper we have assumed at all times that the membrane will remain continuous and intact in the presence of the nanopits, i.e. that the membrane will not rupture or form defects in order to avoid regions of high curvature. Is this assumption justified? As an example, let us consider a nanopit with a strongly curved rim with radius $R_{\rm rim}$ R such as the one in Fig. 2. The energetic cost for the membrane to be bound to this rim can be approximated as a quarter of the bending energy of a

cylinder with radius R_{rim} and length $2\pi R$, giving $E_{\text{be,rim}} \approx \left(\pi^2 / 2\right)\kappa\left(R / r_{\text{rim}}\right)$. On the other hand, if the membrane ruptured in order to avoid adhering to said rim, this process would require the formation of two membrane edges of length close to $2\pi R$, with an energetic cost $E_{\text{edg}} \approx \lambda_{\text{edg}} 4\pi R$, where λ_{edg} is an edge tension or edge energy per unit area. (29) The typical value for such an edge tension, found in experiments and simulations, is about $\lambda_{\text{edg}} \quad 10 \text{ pN} = 10^{-20} \text{ J / nm}$. (35) Rupture of the membrane in order to avoid the highly curved rim will be energetically favored whenever $E_{\text{edg}} < E_{\text{be,rim}}$, which results in the condition $r_{\text{rim}} < \left(\pi / 8\right)\left(\kappa / \lambda_{\text{edg}}\right)$, implying that indeed the membrane prefers to rupture at very strongly curved regions. However, introducing the typical values for λ_{edg} and the bending rigidity $\kappa \quad 10^{-19}$ J, we find $r_{\text{rim}} < 3.9$ nm. As a consequence, we expect that rupture of the membrane will only be preferred at extremely sharp 'kinks' of the substrate, with curvature radii comparable to the thickness of the membrane itself.

Multicomponent membranes

Above, we have focused on laterally-homogeneous membranes with a symmetric bilayer, i.e. on membranes that can be described as having the same bending rigidity κ and zero spontaneous curvature $m = 0$ everywhere. Strictly, such a description should be expected to apply only to membranes consisting of a single lipid species or a mixture of very similar lipids. In general, however, biomembranes may be composed of many different lipids and membrane proteins. These individual components may have different affinities toward the substrate or different preferred curvatures, leading to adhesion- or curvature-induced enrichment or depletion of certain components in specific regions. The compositions of the two monolayers that make the bilayer may vary independently, leading to a spatially inhomogeneous spontaneous curvature of the membrane. (36) Moreover, the different components can genuinely phase-separate, forming well-defined domains of one phase in a surrounding matrix of the other phase, with each phase having different curvature-elastic and adhesive properties. Indeed, model membranes with as little as three components can phase-separate into two macroscopic fluid phases, a liquid-ordered (Lo) and a liquid-disordered (Ld) phase. (37) What effect will this added complexity have on the adhesion of biomembranes to substrates patterned with nanopits?

CA states will still be always (meta)stable, given that this behavior is independent of the material parameters of the membrane, and therefore independent of the details of the local membrane composition at the bottom of the nanopit. The stability limits of NA and PA states, however, will depend on how the membrane components self-organize around the nanopit, and thus on the details of the membrane composition. The basic qualitative result that for weak adhesion NA or PA states are energetically preferred, whereas for sufficiently strong adhesion CA states are preferred, will remain valid independently of the compositional complexity of the membrane. However, the specific values of adhesion at which each state becomes energetically preferred may shift due to a multitude of effects. For example, if some of the membrane components have non-zero preferred curvatures, the cost of bending the membrane in order to adapt to the nanopit shape will be lowered, and CA states will be favored by enrichment of these components near the nanopit. Similarly, CA states may be favored by the existence of phase-separated domains, because adhesion of the domains to the nanopits will reduce the length of the domain boundary and therefore the line tension energy of the system. On the other hand, if a membrane were composed of a mixture of lipids, some of which are attracted to the substrate while others are not (or are repelled from the substrate), we would expect NA states to be favored, because in this way the latter components may avoid the substrate by accumulating in the non-adhered regions of the membrane above the nanopits. One may think of many other factors that will similarly favor one state over the other two: due to the high dimensionality of the parameter space, developing a general theory of adhesion of multicomponent membranes to nanopit-patterned substrates is a difficult task.

Ignoring the *transitions* between states, however, one may ask how the presence of the nanopits will affect the lateral organization of the membrane components. Membranes in a CA state and

membranes in a NA state will behave rather differently in this regard. In a CA state, the whole membrane is adjacent to the substrate, but the curvature of the membrane is non-uniform. In this case, the different membrane components may reorganize to adapt to this non-uniform curvature. Experiments with lipid bilayers made from ternary mixtures supported on undulated substrates with weakly curved plateaus and strongly curved grooves have shown that the more rigid Lo domains will localize at the plateaus and avoid the grooves. (38) Theoretical modelling of the same system (39) shows that localization of Lo domains will occur if the length scale given by $(\kappa_{\mathrm{o}} - \kappa_{\mathrm{d}})/\lambda$ exceeds a certain critical value related to the topographical features of the system (here, κ_{o} and κ_{d} are the bending rigidities of the Lo and Ld phase and λ is the line tension of the domain boundary). Otherwise, the membrane will 'ignore' the topography of the substrate and simply phase-separate into two large domains. This implies that localization will occur only if the rigidity contrast between the two phases is sufficiently large or the line tension is sufficiently small. A similar result may be expected to hold for a nanopit-patterned substrate, with rigid Lo domains avoiding the nanopits and localizing at the flat regions between them.

In a NA state, on the other hand, the whole membrane is flat, but now some regions of the membrane are adjacent to the substrate while others are not. This will lead to reorganization of the membrane components depending on their affinity towards the substrate, with high affinity components being enriched in the adhering region outside the nanopits, and low affinity components being enriched in the non-adhering regions above the nanopits. Once again focusing on phase-separating mixtures, theoretical studies have shown that, in such a situation, domain formation can either occur in the non-adhering regions or in the adhering regions, but never in both. (40, 41) In experiments with pore-spanning membranes, which are in a sense analogous to NA/PA states, Lo domains were observed to be confined to the non-adhering regions of the membrane above the pores. (42)

Nanopit shapes: Limitations and generalizations

As described in *Methods*, throughout this paper we have focused on nanopits with a smooth axisymmetric shape that satisfies certain conditions: The defining height function $z_{\mathrm{np}}(r)$, defined on the interval $0 \leq r \leq R$, was taken to be (i) non-decreasing with only one inflection point in its domain, (ii) differentiable at least once, and satisfying (iii) $z'_{\mathrm{np}}(0) = 0$ and (iv) $z'_{\mathrm{np}}(R) = 0$.

Condition (i) ensured that the nanopit has a simple shape with a single minimum, whereas conditions (ii–iv) ensured the smoothness of the shape, i.e. the absence of 'kinks' on the nanopit surface. We found that the adhesion of membranes to any such nanopit presents a number of universal features, namely that CA states are always metastable (see Eq. 11); that NA states become unstable at a tension-independent critical adhesive strength (see Eqs. 12 and 16); that the instability of NA states can be continuous towards PA states, or discontinuous towards CA states at low membrane tension if the nanopit shape satisfies certain condition (see Eqs. 13 and 14); and finally that PA states become unstable discontinuously towards CA states at a tension-dependent adhesive strength (see Eqs. 15 and 17). If the nanopit shape 'breaks' some of the conditions (i–iv), the adhesion of the membrane to the nanopit will no longer exhibit all these features, as discussed below.

First, let us consider a nanopit that breaks condition (iii), i.e. that has a 'kink' at its bottom, such as the cone-shaped nanopit displayed in Fig. 7(a). In this case, CA states are no longer (meta)stable always: in fact, CA states become strictly impossible, because the membrane cannot adapt its shape to the kink without rupturing or forming a defect. Increasing values of the adhesive strength $|W|$ will therefore only lead to more deeply-adhered PA states. For the particular case of a tensionless membrane in contact with a cone-shaped nanopit such as the one in Fig. 7(a), scale invariance of the bending energy implies that the shape and energy of the unbound segment are independent of the contact radius r^*, and therefore that the adhesion process is governed by the competition between adhesion and bending in the bound segment, with the equilibrium condition $|W| = 2\kappa M_{\mathrm{np}}^2(r^*)$. The mean curvature of the nanopit at the contact line is given by $M_{\mathrm{np}}(r^*) = \sin\alpha / 2r^*$, where α is the

Figure 7: More general nanopit shapes (in black) that 'break' some of the conditions that we imposed in the *Methods* section: (a,b) Nanopits may be non-smooth and instead display a 'kink', which may be located (a) at the bottom, (b) at the rim, or elsewhere along the surface of the nanopit. (c) Nanopits may have 'wiggly' shapes with more than one inflection point along their profile. (d) Nanopits may be non-axisymmetric. In (a–d), the membrane is depicted in blue.
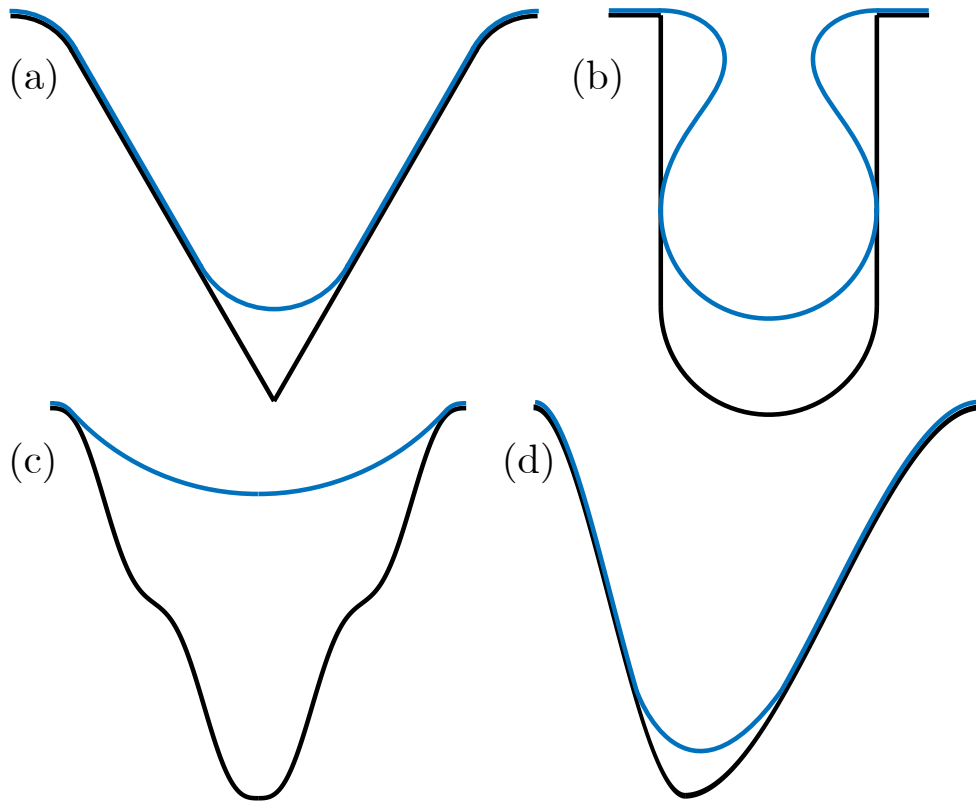
angle of the cone with the horizontal. We therefore find $r^* = \sin\alpha\sqrt{\kappa / 2\,|W|}$, implying that a continuous increase of $|W|$ leads to a continuous decrease of r^*, i.e. to more deeply-adhered PA states, without ever reaching the CA state with $r^* = 0$.

Alternatively, a nanopit may break condition (iv) and have a 'kink' at the rim, such as the cylindrical nanopit displayed in Fig. 7(b). In this case, we expect NA states to be always (meta)stable, i.e. there will not be a critical adhesive strength above which the NA state becomes unstable. The reason is that, in order to adhere to the inside of the nanopit, the membrane will have to first bend into it (which implies both a bending and tension energy cost), without a concomitant gain in adhesion energy. There will therefore always be an energy barrier separating the NA state from the PA or CA states, independently of the adhesive strength of the substrate. We have used the numerical shooting method (described in *Methods*) to calculate the shape of a tensionless membrane when bending into a cylindrical nanopit with a $90°$ 'kink' at the rim, see the blue line in Fig. 7(b). The membrane must develop an 'overhang' in order to avoid the rim and still adhere to the walls. The state depicted corresponds to the 'top' of the energy barrier, with a barrier height given by $0.9 \times 8\pi\kappa$, of the order of several hundred $k_{\mathrm{B}}T$ for a typical bending rigidity. This energy barrier will be even higher for membranes under tension. However, the energy barrier will be smaller (but still non-zero) for shallower nanopits, either with non-vertical walls, or with sufficiently short vertical walls, in which case the membrane will make initial contact with the bottom rather than the walls of the nanopit. Similar considerations will come into play if condition (ii) for the nanopit shape is broken, i.e. if the nanopit displays a 'kink' somewhere between its bottom and its rim.

In Fig. 7(c), we display a nanopit with a 'wiggly' shape that breaks condition (i), in that its height function $z_{\mathrm{np}}(r)$ has more than one inflection point in its domain, namely three in this case. This implies that the principal curvature of the nanopit that is perpendicular to the contact line changes sign three times, instead of just once. The fact that CA states are always (meta)stable and the existence of a tension-independent stability limit of the NA state remain unchanged independently of the number of inflection points, because our derivation of Eqs. 11–12 depended only on the local shape of the nanopit at the bottom or at the rim. However, we can show that in this case two or more distinct (meta)stable PA states will coexist with each other and with the CA state at sufficiently large membrane tensions. This can be directly inferred, in the limit of large tension, from the same argument that led to Eq. 15, because in this case $|W|$ will have n maxima as a function of r^* when the height function has $2n-1$ inflection points. The same conclusion can be reached, without recurring to the limit of large tension, for the special case of 'stair-like' nanopits constructed from a smooth combination of cylindrical and toroidal segments, using the same arguments that led to Eqs. 17–19. We note, however, that we have not rigorously established the relation between the number of inflection points and the number of coexisting PA states, at low tensions, for nanopits of general shape.

Finally, it is also possible to relax the condition of axisymmetry, as in the non-axisymmetric example of Fig. 7(d). Both the numerical shooting method as well as the analytical small gradient approximation used in this work (see *Methods*) were based on the assumption of axisymmetry, and are thus not applicable to such nanopits. We can, however, make some educated guesses. First, we still expect NA states to be in general stable for sufficiently low adhesive strength, and to become unstable above a tension-independent critical adhesive strength. At the rim of a non-axisymmetric nanopit, the curvature C_{rim} perpendicular to the line where the nanopit meets with the flat substrate is no longer a constant and instead varies along the length of this line. Given that the contact curvature condition in Eq. 3 is valid for non-axisymmetric geometries, and that in the NA state the unbound membrane is completely flat with $C_\perp \equiv 0$, we may expect the NA state to become unstable for adhesive strengths above $|W| = \min\left(\kappa C_{\mathrm{rim}}^2 / 2\right)$, i.e. to be governed by the weakest rim curvature along the length of the contact line between the nanopit and the flat substrate. Second, we may wonder whether the fact that CA states are always (meta)stable remains valid. It is tempting to

speculate that it will, as long as the bottom of the non-axisymmetric nanopit is smooth. However, it is also possible that the adhesive strength threshold for (meta)stability of the CA state is proportional to a measure of the local deviation from axisymmetry at the bottom of the nanopit, such as $|W| \propto \kappa \left(M_b^2 - K_b \right)$, where M_b and K_b are the mean and Gaussian curvatures at the bottom of the nanopit, which would still result in $|W| = 0$ for axisymmetric nanopits. Establishing this will presumably require a more general framework suited to non-axisymmetric geometries, such as the one used in Ref. 23.

Conclusion

In summary, we have shown that the adhesion of biomembranes to substrates topographically patterned with nanopits displays many universal features that are independent of the detailed shape of the nanopits. We have provided conditions for the stability of non-, partially- and completely-adhered states valid for a very general class of nanopit shapes, see Eqs. 11–15, as well as for the special case of cylindrical nanopits with vertical walls, see Eqs. 16–17. These conditions can be applied as guidelines to the design and analysis of experiments involving vesicles, supported bilayers, or cells in contact with nanopits. Furthermore, we have examined the coarse-grained effect of many nanopits on membrane–substrate adhesion. The presence of nanopits couples the tension of the membrane to the effective adhesiveness of the substrate, which should display hysteresis in response to cycles of increasing and decreasing tension. Nanopits can lead to both an increase or a decrease in the effective substrate adhesiveness, depending on the relative values of the real adhesive strength $|W|$ of the substrate and the membrane tension Σ, see Eq. 22. We have described in detail how our results relate to the existing experimental evidence for supported lipid bilayers and biological cells in contact with substrates topographically patterned with nanopits, and furthermore we have proposed an explicit way to test our results in experiments using micropipette-held giant vesicles in contact with such substrates. We have also discussed how the presence of nanopits may affect the integrity of the membrane, as well as the lateral organization of the different membrane components in the case of multicomponent membranes. Finally, we have pointed to exciting new directions in the theoretical and experimental study of membrane adhesion to nanopits with more complex shapes.

As a final remark, it is worth noting that, besides nanopits, our results may be used to describe the entry and migration of membranes into cylindrical nanopores. In this case, partially-adhered states will become unstable towards growth of a membrane protrusion into the pore. The stability limit of the partially-adhered state will nevertheless still be given by Eq. 17. For a description of cell migration through micron-sized pores, however, deformations of the cellular cortex and active cytoskeletal forces as well as osmotic pressure effects are expected to become important.

Author Contributions

J.A-C. and D.E.D. designed the research; J.A-C. performed the research; J.A-C. wrote the first draft; J.A-C. and D.E.D discussed and edited the manuscript.

Acknowledgments

References

1. Norman, J. J., and T. A. Desai, 2006. Methods for fabrication of nanoscale topography for tissue engineering scaffolds. *Ann. Biomed. Eng.* 34:89–101.

2. Stevens, M. M., and J. H. George, 2005. Exploring and engineering the cell surface interface. *Science* 310:1135–1138.

3. Bettinger, C. J., R. Langer, and J. T. Borenstein, 2009. Engineering substrate topography at the Micro- and nanoscale to control cell function. *Angew. Chemie - Int. Ed.* 48:5406–5415.

4. Anselme, K., P. Davidson, A. M. Popa, M. Giazzon, M. Liley, and L. Ploux, 2010. The interaction of cells and bacteria with surfaces structured at the nanometre scale. *Acta Biomater.* 6:3824–3846.

5. Kim, D. H., P. P. Provenzano, C. L. Smith, and A. Levchenko, 2012. Matrix nanotopography as a regulator of cell function. *J. Cell Biol.* 197:351–360.

6. Jeon, H., S. Koo, W. M. Reese, P. Loskill, C. P. Grigoropoulos, and K. E. Healy, 2015. Directing cell migration and organization via nanocrater-patterned cell-repellent interfaces. *Nat. Mater.* 14:918–923.

7. Vogel, V., and M. Sheetz, 2006. Local force and geometry sensing regulate cell functions. *Nat. Rev. Mol. Cell Biol.* 7:265–275.

8. Dalby, M. J., N. Gadegaard, R. Tare, A. Andar, M. O. Riehle, P. Herzyk, C. D. W. Wilkinson, and R. O. C. Oreffo, 2007. The control of human mesenchymal cell differentiation using nanoscale symmetry and disorder. *Nat. Mater.* 6:997–1003.

9. Richert, L., F. Vetrone, J. H. Yi, S. F. Zalzal, J. D. Wuest, F. Rosei, and A. Nanci, 2008. Surface nanopatterning to control cell growth. *Adv. Mater.* 20:1488–1492.

10. Biggs, M. J. P., R. G. Richards, N. Gadegaard, R. J. McMurray, S. Affrossman, C. D. W. Wilkinson, R. O. C. Oreffo, and M. J. Dalby, 2009. Interactions with nanoscale topography: Adhesion quantification and signal transduction in cells of osteogenic and multipotent lineage. *J. Biomed. Mater. Res. A* 91:195–208.

11. Zhao, W., L. Hanson, H. Y. Lou, M. Akamatsu, P. D. Chowdary, F. Santoro, J. R. Marks, A. Grassart, D. G. Drubin, Y. Cui, and B. Cui, 2017. Nanoscale manipulation of membrane curvature for probing endocytosis in live cells. *Nat. Nanotechnol.* 12:750–756.

12. Swain, P. S., and D. Andelman, 1999. The Influence of Substrate Structure on Membrane Adhesion. *Langmuir* 15:8902–8914.

13. Swain, P. S., and D. Andelman, 2001. Supported membranes on chemically structured and rough surfaces. *Phys. Rev. E* 63:051911.

14. Decuzzi, P., and M. Ferrari, 2010. Modulating cellular adhesion through nanotopography. *Biomaterials* 31:173–179.

15. Pfeiffer, I., B. Seantier, S. Petronis, D. Sutherland, B. Kasemo, and M. Zäch, 2008. Influence of nanotopography on phospholipid bilayer formation on silicon dioxide. *J. Phys. Chem. B* 112:5175–5181.

16. Pfeiffer, I., S. Petronis, I. Köper, B. Kasemo, and M. Zäch, 2010. Vesicle adsorption and phospholipid bilayer formation on topographically and chemically nanostructured surfaces. *J. Phys. Chem. B* 114:4623–4631.

17. Samiee, K., J. Moran-Mirabal, Y. Cheung, and H. Craighead, 2006. Zero Mode Waveguides for Single-Molecule Spectroscopy on Lipid Membranes. *Biophys. J.* 90:3288–3299.

18. Lee, I.-H., H. Kai, L.-A. Carlson, J. T. Groves, and J. H. Hurley, 2015. Negative membrane curvature catalyzes nucleation of endosomal sorting complex required for transport (ESCRT)-III assembly. *Proc. Natl. Acad. Sci. U. S. A.* 112:15892–15897.

19. Seifert, U., K. Berndl, and R. Lipowsky, 1991. Shape transformations of vesicles: phase diagram for spontaneous-curvature and bilayer-coupling models. *Phys. Rev. A* 44:1182–1202.

20. Seifert, U., and R. Lipowsky, 1990. Adhesion of vesicles. *Phys. Rev. A* 42:4768–4771.

21. Morris, C. E., and U. Homann, 2001. Cell surface area regulation and membrane tension. *J. Membr. Biol.* 179:79–102.

22. Sens, P., and J. Plastino, 2015. Membrane tension and cytoskeleton organization in cell motility. *J. Phys. Condens. Matter* 27:273103.

23. Deserno, M., M. M. Müller, and J. Guven, 2007. Contact lines for fluid surface adhesion. *Phys. Rev. E* 76:011605.

24. Deserno, M., 2004. Elastic deformation of a fluid membrane upon colloid binding. *Phys. Rev. E* 69:031903.

25. Agudo-Canalejo, J., and R. Lipowsky, 2016. Stabilization of membrane necks by adhesive particles, substrate surfaces, and constriction forces. *Soft Matter* 12:8155–8166.

26. Das, S., and Q. Du, 2008. Adhesion of vesicles to curved substrates. *Phys. Rev. E* 77:011907.

27. Zhang, J., S. Das, and Q. Du, 2009. A phase field model for vesicle-substrate adhesion. *J. Comput. Phys.* 228:7837–7849.

28. Cremer, P. S., and S. G. Boxer, 1999. Formation and Spreading of Lipid Bilayers on Planar Glass Supports. *J. Phys. Chem. B* 103:2554–2559.

29. Lipowsky, R., and U. Seifert, 1991. Adhesion of Vesicles and Membranes. *Mol. Cryst. Liq. Cryst.* 202:17–25.

30. Lipowsky, R., 2014. Coupling of bending and stretching deformations in vesicle membranes. *Adv. Colloid Interface Sci.* 208:14–24.

31. Evans, E., D. Berk, and A. Leung, 1991. Detachment of agglutinin-bonded red blood cells. I. Forces to rupture molecular-point attachments. *Biophys. J.* 59:838–848.

32. Prechtel, K., A. R. Bausch, V. Marchi-Artzner, M. Kantlehner, H. Kessler, and R. Merkel, 2002. Dynamic Force Spectroscopy to Probe Adhesion Strength of Living Cells. *Phys. Rev. Lett.* 89:028101.

33. Brochard-Wyart, F., and P. D. Gennes, 2003. Unbinding of adhesive vesicles. *Comptes Rendus Phys.* 4:281–287.

34. Colbert, M. J., A. N. Raegen, C. Fradin, and K. Dalnoki-Veress, 2009. Adhesion and membrane tension of single vesicles and living cells using a micropipette-based technique. *Eur. Phys. J. E* 30:117–121.

35. Jiang, F. Y., Y. Bouret, and J. T. Kindt, 2004. Molecular dynamics simulations of the lipid bilayer edge. *Biophys. J.* 87:182–192.

36. McMahon, H. T., and J. L. Gallop, 2005. Membrane curvature and mechanisms of dynamic cell membrane remodelling. *Nature* 438:590–596.

37. Marsh, D., 2010. Liquid-ordered phases induced by cholesterol: a compendium of binary phase diagrams. *Biochemistry* 1798:688–699.

38. Parthasarathy, R., C.-h. Yu, and J. T. Groves, 2006. Curvature-Modulated Phase Separation in Lipid Bilayer Membranes. *Langmuir* 22:5095–5099.

39. Rózycki, B., T. R. Weikl, and R. Lipowsky, 2008. Stable patterns of membrane domains at corrugated substrates. *Phys. Rev. Lett.* 100:098103.

40. Lipowsky, R., T. Rouhiparkouhi, D. E. Discher, and T. R. Weikl, 2013. Domain formation in cholesterol–phospholipid membranes exposed to adhesive surfaces or environments. *Soft Matter* 9:8438–8453.

41. Rouhiparkouhi, T., T. R. Weikl, D. E. Discher, and R. Lipowsky, 2013. Adhesion-induced phase behavior of two-component membranes and vesicles. *Int. J. Mol. Sci.* 14:2203–2229.

42. Orth, A., L. Johannes, W. Römer, and C. Steinem, 2012. Creating and modulating microdomains in pore-spanning membranes. *ChemPhysChem* 13:108–114.